energies

MDPI

Article

A Quasi-Steady State Model of a Solar Parabolic Dish Micro Gas Turbine Demonstration Plant

Michela Lanchi [1,*], Jafar Al-Zaili [2], Valeria Russo [1], Massimo Falchetta [1], Marco Montecchi [1] and Lukas Aichmayer [3]

[1] ENEA—Italian National Agency for New Technology, Energy and Sustainable Economic Development, Casaccia Research Centre, Via Anguillarese 301, S. Maria di Galeria, 00123 Rome, Italy; valeria.russo@enea.it (V.R.); massimo.falchetta@enea.it (M.F.); marco.montecchi@enea.it (M.M.)

[2] Department of Mechanical Engineering and Aeronautics, City University of London, Northampton Square, London EC1V 0HB, UK; jafar.alzaili@city.ac.uk

[3] Department of Energy Technology, KTH Royal Institute of Technology, SE-100 44 Stockholm, Sweden; lukas.aichmayer@energy.kth.se

* Correspondence: michela.lanchi@enea.it; Tel.: +39-(06)-30483292

Abstract: In the framework of the European Optimised Microturbine Solar Power system (OMSoP) project, a novel energy system for solar electricity production was developed, based on the integration of the solar dish technology with Micro Gas Turbines (MGT). A pilot plant with a capacity of 5–7 kW_e was realized and installed at the ENEA Casaccia site (Rome) and went under testing to validate the feasibility of the technology and improve the current design. The present work deals with the development of a quasi-state system model, built in the Engineering Equation Solver environment, composed of different modules that correspond to the main system components. The system model was used to define the optimal system parameters, to help the elaboration on an operational strategy to maximize the overall plant efficiency, and to guide the improvement of the single components in view of their optimised design. From the analysis it emerged that the system in design conditions is able to generate, in nominal conditions, 4.5 kW_e instead of the expected 5 kW_e due to the limitation of the stator current to 13 A, while maximum levels of 5.6 kW could be achieved by "overcharging" the high-speed generator up to 15 A and operating the MGT at the very high speed of 150 krpm. From the transient simulation of the demo system on an annual basis, the maximum average output power is 3.58 kW_e. Regarding the cycle efficiency, the annual averaged value is about 17%, whereas the target value is 21%. The improvement of the generator only does not seem to significantly increase the power output on the annual basis (3.75 kW_e vs. 3.58 kW_e). Differently, the improvement of the solar dish, with the upgrade of the other system components, would significantly increase the system power output to around ~10 kW_e.

Keywords: concentrated solar power plants; solar dish; micro gas turbine; stationary system model

Citation: Lanchi, M.; Al-Zaili, J.; Russo, V.; Falchetta, M.; Montecchi, M.; Aichmayer, L. A Quasi-Steady State Model of a Solar Parabolic Dish Micro Gas Turbine Demonstration Plant. *Energies* **2022**, *15*, 1059. https://doi.org/10.3390/en15031059

Academic Editor: Jesús Polo

Received: 14 December 2021
Accepted: 23 January 2022
Published: 31 January 2022

1. Introduction

Due to the increasing global population and growing electricity demand, the development of new sustainable energy technologies has become of crucial importance to reduce emissions of carbon dioxide and other greenhouse gases. The Concentrated Solar Power (CSP) technology, which uses the heat generated by concentrating and absorbing the sun's energy to drive a heat engine/generator, can be considered one of the more viable and promising routes for renewable electricity production. Indeed, CSP technology, through thermal energy storage, can provide a dispatchable electrical output. As result, CSP systems are suitable for balancing the fluctuating output of other renewable technologies [1], which is becoming a crucial issue. The increasing penetration of intermittent renewable energy sources, such as solar photovoltaics and wind into the production mix (currently 13% in

Italy and Sweden, 18% in Spain and up to 27% in Denmark) is becoming an important challenge to maintain the stability of the electricity grid.

CSP technology can be targeted both for high-capacity power plants, through the use of parabolic trough and solar tower systems, and for small-capacity applications, through the adoption of dish systems. Large-scale Solar Thermal (STE) power systems, which benefit from significant economies of scale [2], are now a consolidated technology with a total installed capacity over 5 GW_e worldwide [3]. However, small-scale solar thermal power systems, ranging in size from a few kW to some MW, have not entered the market of distributed generation since they must compete against the low cost, ease of operation and reliability of photovoltaic technology [4]. This has been the case for the dish technology coupled with Stirling engines, whereby a parabolic dish collector tracks the sun and focuses solar energy onto a heat engine/generator to produce electric power [5–7]. Dish-Stirling systems have been developed in the United States and Europe since the early 1980s, and several demonstration systems have been built and operated in pre-commercial applications, ranging from 2 to 50 kW [8]. Nevertheless, the high cost of the components (dish/engine), the high operating and maintenance costs of the Stirling engine using hydrogen as process fluid at almost 200 bar, and the low technology manufacturing level led to a final cost of electricity exceeding 0.30–0.35 USD/kWh [2,4].

Taking into account this scenario, an innovative system for distributed electricity production was proposed to possibly overcome the main limitations of the Dish/Stirling technology. This new technology is based on the replacement of the Stirling engine with a micro gas turbine (MGT) with the aim of increasing the system reliability and operability in relation to solar energy short time fluctuations [9]. The development of such a system was financed by the European Commission through the OMSoP project (Optimised Microturbine Solar Power system), which started in 2013 and finished in 2017, involving a consortium of European companies and research institutions [10–13].

The adoption of an MGT coupled with the dish technology is a substantial innovation in the CSP field but is in line with a growing attention towards the solar gas turbine application, including solar/fuel hybrid configurations [14–17]. In fact, in the past decade, different projects focusing on the integration of gas turbines with solar plants were supported by the European Commission. In particular, within the SOLGATE project [18], a solar-powered gas turbine in a hybrid configuration (250 kW_e) was demonstrated, while the SOLHYCO project developed a 100 kW_e co-generative unit with a new biofuel combustion system [19]. These activities have led to a number of other projects such as SOLUGAS [20], where a hybrid solar gas turbine was operated at MW scale, and PEGASE [21], which aimed at setting up and testing a solar power demonstrator of 1.4 MW. More recently, SolGATS, a research collaboration between academic institutions and industries from the UK and China, has studied the potential of the CSP MGTs integrated with thermal energy storage [22,23]. The focus of the project was mainly off-grid applications in rural areas.

Therefore, even if the technical feasibility of MW-scale power plants has been investigated so far, the adoption of micro gas turbines powered by the solar source for distributed electricity production in remote areas is quite a new perspective. To verify the feasibility of the integration between the dish technology and the MGTs, a full-scale demonstration plant with a capacity of 5 kW_e was realized within the OMSoP project. The facility was installed at the ENEA Casaccia site, near Rome, and was commissioned in 2017. The system, represented in Figure 1, principally consists of a solar dish concentrator, a receiver and an MGT. The solar receiver, positioned in correspondence of the focal point of the dish, absorbs the concentrated radiation and transfers it to a compressed air flow, which is then processed by the MGT for producing mechanical work, through a recuperated Brayton cycle, with an operative pressure of 3 atm and a maximum temperature of 900 °C.

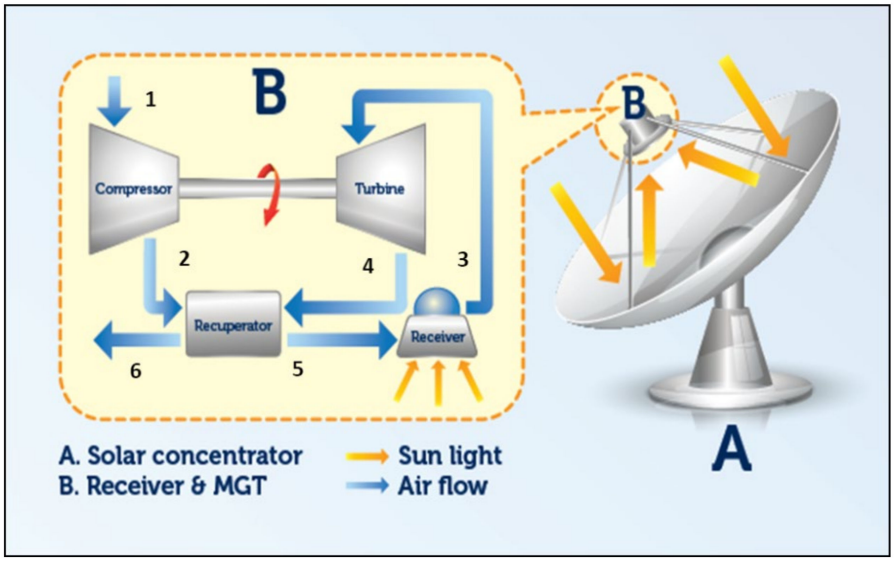

Figure 1. Scheme of the Optimised Microturbine Solar Power system (OMSoP) process.

The research effort was focused both on the development of highly efficient and reliable components, capable of withstanding high temperature levels (800–900 °C) and unstable operative conditions, and on the selection of the optimum integration solution for the MGT and the solar dish. Furthermore, research was focused on developing proper operation strategy for maximizing the overall plant efficiency, depending on the meteorological conditions. To this purpose a system model, capable of predicting the plant behaviour at different meteorological conditions, namely Direct Normal Irradiance (DNI) and ambient temperature and pressure, was developed by ENEA. The present work deals with this modelling activity carried out during the course of the OMSoP project with the aim of (1) defining the optimal system parameters, (2) conceiving an operation strategy to maximize the overall plant efficiency and (3) guiding the improvement of the single components. In particular, the present work describes the modelling process and provides the results of the model application in terms of system performance prediction, with a particular attention to the limiting factors to be overcome in a future design revision of the system. Many valuable works published in the recent years deal with dish-MGT system models to optimise and assess the performance of this technology from a global perspective [24,25]. Distinguished from other work, the present study is based on a real-scale prototype, and consequently the analysis is supported by the direct experience of technical issues and practical limitations, which typically are not taken into consideration in academic and theoretical analyses. In this regard, in the present paper, the technical problems and limitations encountered both in the design of the single components and in their integration are presented. Particularly, as an example of technical limitations evidenced during the course of the project, it is worth mentioning (i) the mismatch between the concentrated power intercepted by the receiver and the power required by the MGT, and (ii) the stator current limitation of the high-speed generator, which led to an electrical power output lower than the nominal one. Through the analysis and/or testing of each component, the main bottlenecks of the investigated technology were identified and corrective design actions were conceived.

2. Methodology

2.1. System Model Development

The demo system model, which was iteratively modified and refined during the course of the OMSoP project, was implemented in the EES environment (Engineering Equation Solver) to build a customized tool for quasi-steady state simulations. The demo model was assembled through the integration of different modules, corresponding to the main system components, each represented as a box described by characteristic equations

or performance maps. Each component model was separately implemented and then integrated into the whole system through heat and mass balance equations. The final version of the demo model is described in the present document, taking into account the latest updates on the components' operating conditions and specifications (Table 1).

Table 1. Demo system nominal operating conditions and main component specifications.

Dish		**Receiver (Cavity/Volumetric)**	
External diameter [m]	11.70	Window diameter [cm]	22.00
Internal diameter [m]	2.12	Thermal efficiency	0.70–0.85
Nominal aperture area (m^2)	108.00	Pressure drop [%]	2.00
Effective aperture area (m^2)	88.00	Mass flow rate [kg/s]	0.07
Power intercepted [kW]	70.44	Power at the rec. window [kW]	30.40
Power at the focal plane [kW]	62.19	Net power absorbed [kW]	21–25
Recuperator		**MGT**	
Combined pressure drop	5%	Compressor Inlet Temperature [°C]	15
Effectiveness	85%	Turbine Inlet temperature [°C]	800
Weight [kg]	50	Compressor Pressure Ratio	2.90
HSG		Compression efficiency [%]	74.00
Rated speed [krpm]	130	Mechanical efficiency [%]	95.00
Rated Power [kW]	6	Turbine efficiency [%]	81.50
Rated voltage [V]	338	n [krpm]	100/130
Maximum speed [krpm]	150	Mechanical Power Produced [kW]	5.00

The model was developed based on validated components' models as described in the following subsections. The system consists of three main subsystems, namely the dish, the receiver and the MGT, as illustrated in Figure 1. The models developed for the three subsystems were validated against the experimental data. A new tool was developed by [26] to characterise the solar dish and to measure its optical efficiency. The details are provided in Section 2.2. The solar dish was installed, characterised and tested by ENEA, one of the partners in the OMSoP project, which was responsible for the demonstration activities. The model developed for the solar dish was adopted in the system model. The solar receiver was designed and tested in a laboratory setup as discussed in [27] by one of the OMSoP project partners, KTH. This was the same receiver used in the demonstration plant. In the current model, the receiver was characterised by its efficiency, pressure drop and temperature rise. These parameters were taken from the experimental data provided by [27] as discussed in Section 2.3. The MGT, including the generator, was designed and tested at the laboratories of City University of London. Extensive experimental and simulation investigations were undertaken to characterise the MGT. The results are provided in [28–30] and were adopted to model the MGT performance in the current system model. The performance map for the turbo-components, the compressor and the turbine was extracted from these investigations and implemented in the current model as discussed in Section 2.4.

2.2. Dish Modelling

The dish, designed and realized by INNOVA, is composed of two circular crowns of mirrors that concentrate sun rays on the solar receiver located on the focus of the paraboloid. The reflecting surface, about 100 m^2, was sized not only to collect the power required by the OMSoP system but also to assure a good margin of flexibility for a possible scale up of the MGT (from 5 kW to 10–15 kW). The focus/diameter ratio is about 0.6, which was demonstrated to be the optimal shape of the parabola to achieve the highest concentration ratio and the highest temperatures [31].

The selected reflecting material is a commercial product, ALMIRR®, a multi-laminar aluminium mirror by Alucoil: this choice was dictated by a compromise solution between durability, cost and performance.

Regarding the dish modelling activity, two different approaches were adopted for predicting the dish performance. Initially, a simplified model, based on the assumption of Gaussian distribution of the solar flux, was developed [11]. Later, once experimental data on the dish features were available, a more rigorous model was implemented in a cross-platform software (Linux, Mac, Windows), written in C++ and linked to the Qt library for the graphical user interface [32]. The SIMUL-DISH software deals the flux calculation by means of a finite element approach where the dish surface can be assumed as parabolic or spherical or can be "customized" by considering the experimental data (x, y, z and slopes) when available. To develop the latter option, the slope deviation of the unit vector normal to the surface element was experimentally evaluated by means of the ENEA VISdish method, described in detail elsewhere [33]. The outcome is summarized in Figure 2, showing the contour map and the distribution of the experimental slope-deviation magnitude, respectively [33]. The distribution is peaked at 5 mrad and ranges from 0 to 20 mrad.

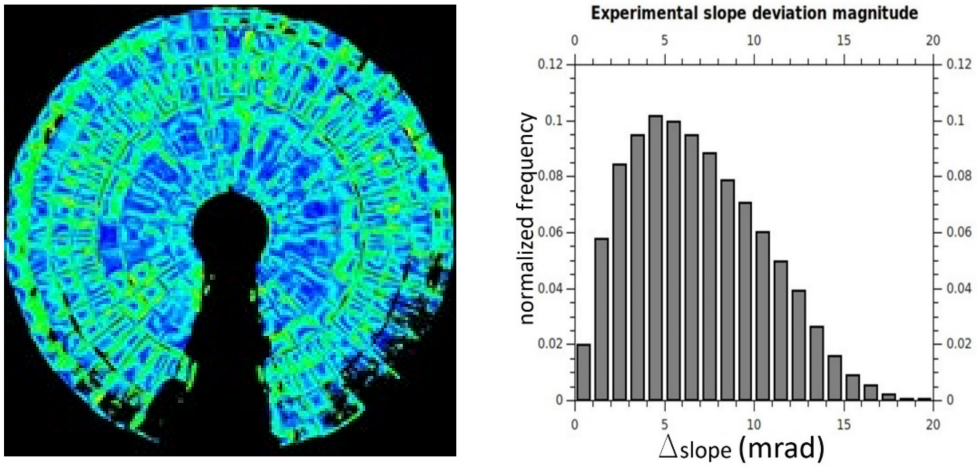

(**a**) (**b**)

Figure 2. (**a**) Contour map of the experimental magnitude of the slope-deviation Δslope. Black = not sampled, pixel-colour from blue to red corresponds to slope-deviation from 0 to 20 mrad [18]; (**b**) Distribution of the slope-deviation magnitude [19].

Concerning the reflectance, Almirr mirror was exhaustively characterized by ENEA through the Solar Mirror Qualification set-up [33]: the results are summarized in Figure 3, showing the behaviour of both solar hemispherical reflectance and the Sun-radiation Conic Reflectance (SCR) versus the incidence angle, for several acceptance angles. SCR is a recently proposed parameter [34], defined as the radiation ratio incident on the receiver window assuming a perfect mirror shape and obtained by integrating the near specular reflectance over the Sun disk; the main peculiarity and advantage of SCR is that it contains the contribution of divergence of the solar radiation.

The experimental data of reflectance and shape were entered and processed by SIMUL-DISH software, getting the main parameters summarized in Table 2 for different receiver-window diameter values:

- Optimal z value, corresponding to the focal distance where the flux shows the highest concentration;
- Maximum Concentration Factor (CF);
- Mean CF;
- Overall optical efficiency, defined as the ratio between the power entering the receiver window and the power intercepted on the mirror surface.

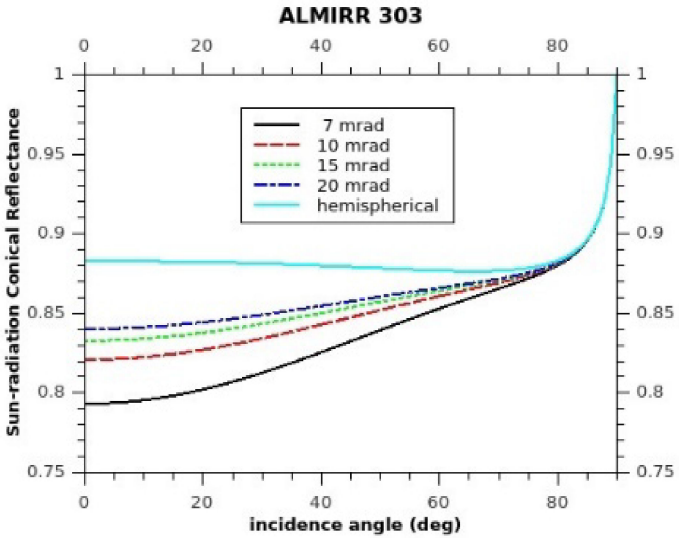

Figure 3. Results of the dish reflectance measurement [19].

Table 2. Calculated OMSoP dish performance.

	Receiver Window Diameter [cm]				
	15	**18**	**21**	**24**	**27**
Effective reflecting area [m^2]	88	88	88	88	88
Optimal z value [m]	7.02	7.02	7.02	7.02	7.02
Maximum CF [suns]	1677	1677	1677	1677	1677
Mean CF [suns]	1216	1096	984	884	793
Optical efficiency	0.258	0.335	0.409	0.480	0.545
Incident Power on the receiver window @800 W/m^2 [kW]	18.17	23.58	28.79	33.79	38.36

The results of the SIMULDISH calculation were included into the system model in form of performance map, where the DNI and the receiver window diameter are the input data and the power delivered to the receiver is the output data.

From Table 2 the limited optical efficiency of the dish can be clearly deduced, since a maximum overall optical efficiency of 54% has been estimated here, whereas a state-of-the art dish can presently reach an optical efficiency of about 80%, corresponding approximately to a total error of 7–8 mrad [35,36]. This result also can be deduced by considering the slope-deviation magnitude measured through the VISdish method (Figure 2b), which in a typical dish system comprises between 1 and 5 mrad: most probably in the OMSoP dish the mirror support had a moulding defect, easily detectable trough a visual inspection, which caused a displacement of the concentrated radiation from the focal point. Although dish efficiency could be increased by enlarging the receiver window diameter, a compromise value for the receiver diameter (0.22 cm) was selected in order to raise the power intercepted by the window without penalizing the concentration factor too much, as presented in the following paragraphs.

2.3. Receiver Modelling

In the framework of the OMSoP project, it was planned to manufacture two different types of receivers (cavity and volumetric), designed and realized by KTH—Royal Institute of Technology (Sweden), in order to have a back-up component in case of failure during the experimental testing and to identify the best design solution. The cavity receiver, produced in metallic alloy, was expected to be more robust but less efficient, whereas the volumetric one, made from ceramic and metallic materials and provided with a quartz window, is more fragile but typically more efficient. Both receivers were considered in the system modelling.

Initially, in absence of design details, a simplified model for the volumetric receiver was developed and implemented in EES [11]. In the final step, once available the receiver performance maps provided by KTH, based on a 2D CFD model and ray tracing tool described elsewhere [37,38], the receiver outlet temperature T_3 was evaluated by means of data interpolation; the input data to the receiver maps are the receiver inlet temperature (T_5), the air mass flow rate ($\dot{m}$) and the DNI, while the outlet parameters are the receiver thermal efficiency (η_r), the receiver outlet temperature (T_3) and the receiver pressure drops (ΔP_r). As an example, in Figure 4 the receiver performance maps (η_r, T_3, ΔP_r varying *DNI* and T_5 at a constant air flow rate of 0.3 kg/s) are reported. These data refer to a receiver window diameter of 21 cm, but similar matrices were built for receiver window diameters in the range of 21–22 cm.

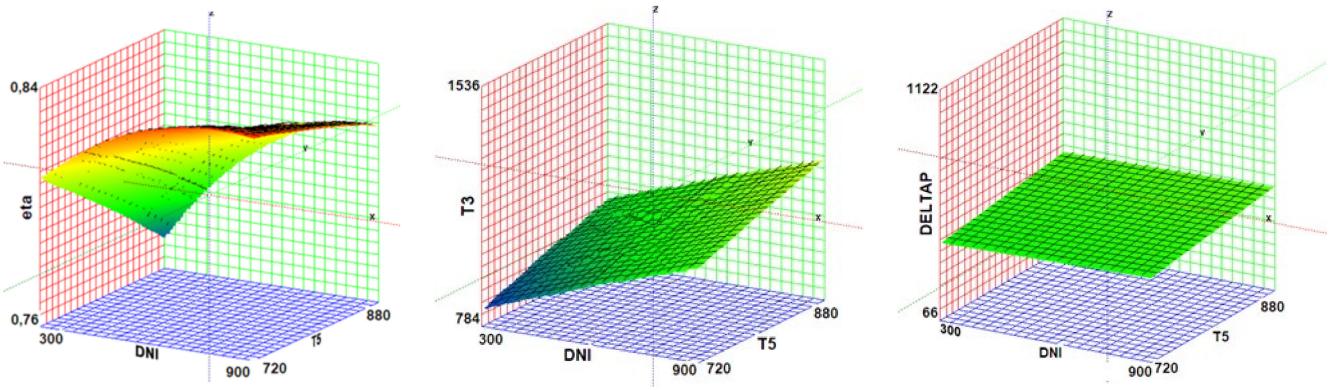

(**a**) (**b**) (**c**)

Figure 4. Receiver performance maps at a constant mass flow rate of 0.3 kg/s: (**a**) receiver thermal efficiency vs. Direct Normal Irradiance (DNI) [W/m^2] and receiver inlet temperature [K]; (**b**) receiver outlet temperature vs. DNI [W/m^2] and receiver inlet temperature [K]; (**c**) receiver pressure drops [Pa] vs. DNI and receiver inlet temperature [K] (derived from draft data from KTH, oral communication).

Regarding the cavity receiver, in the absence of more detailed data, the thermal efficiency η_r was considered constant and equal to 0.7, a realistic value for applications at this high temperature level (800 °C). Therefore, the calculation of the receiver outlet temperature T_3 was accomplished through the Equation (1), with the power absorbed by the air flow P_{net} calculated through the Equation (2):

$$P_{net} = \dot{m} \cdot (h_3 - h_5) \quad (1)$$

$$P_{net} = \eta_r \cdot P_w \quad (2)$$

where h_3 and h_5 are the outlet and the inlet specific air enthalpies, respectively, and P_w is the incident power at the receiver window.

2.4. MGT Modelling

The core of the OMSoP technology, the Micro Gas Turbine, was designed and produced by the City University of London. It is composed of a compressor, a turbine, a recuperator, and a High-Speed Generator (HSG); the turbine shaft work is used to drive the compressor and the electric generator that are coupled to the shaft.

The design process of the MGT, including the one-dimensional analysis, the three-dimensional design, the Computational Fluid Dynamics (CFD) characterization, and the Finite Element Analysis (FEA), are described in [29,30], together with constructive details.

In view of the system model development, performance maps of the turbine and the compressor (Figures 5 and 6, respectively) were provided by City University [39], while for the HSG a stationary model was developed by ENEA, presented in the next paragraph. In

particular the turbo-compressor operating point was individuated by matching the air flow rate $\dot{m}$ and the pressure ratio P_{ratio} and PR, net of the cycle pressure drops.

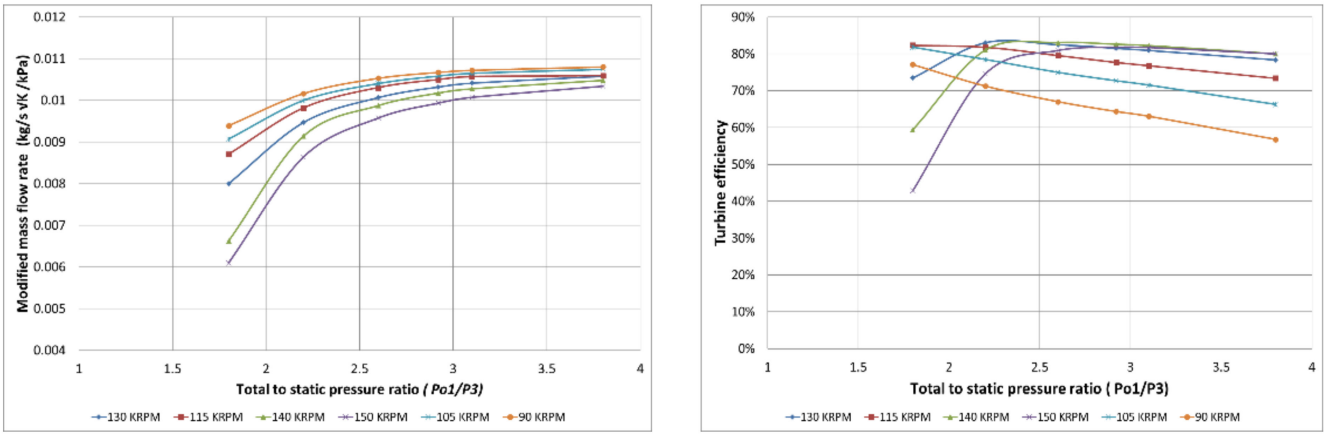

(**a**) (**b**)

Figure 5. (**a**) Turbine performance map; (**b**) Turbine efficiency versus pressure ratio [29].

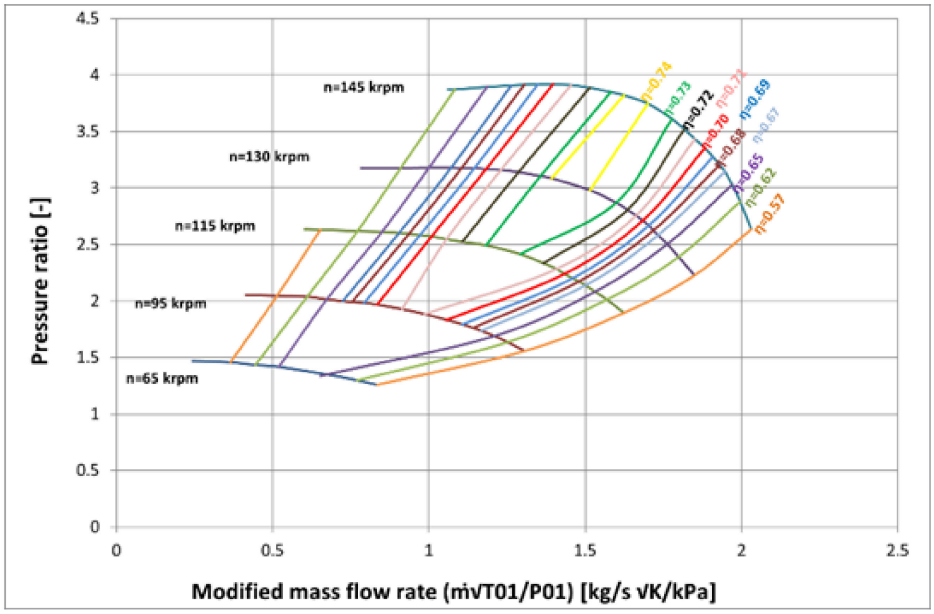

Figure 6. Compressor performance map [29].

Furthermore, since the driving torque and the load torque are perfectly balanced in the steady state condition, the electrical power output P_{ele} is equal to the turbo-compressor net power, as reported in the following relation

$$P_{ele} = (P_t - P_{cm}) \cdot \eta_{ele} \quad (3)$$

where η_{ele} is the electrical efficiency of the HSG, described in the following paragraph, P_t and P_{cm} are the total turbine and the total compressor power, respectively. Concerning the recuperator, it has been assumed, as a preliminary approximation, that the heat exchange efficiency η_{rec} has a stepwise behaviour, being 0.85 for a turbine outlet temperature equal or higher than 160 °C and 0 in correspondence of a temperature lower than 160 °C.

In conclusion, for the MGT integration into the system model, the following heat and mass balance equations were considered (see Figure 1 for the streams notations):

- Compressor

$$P_{cm} = \frac{P_c}{\eta_{mec}} = \frac{\dot{m} \cdot (h_2 - h_1)}{\eta_{mec}} \quad (4)$$

$$\eta_{cm} = \frac{(h_2 - h_1)}{(h_{2is} - h_1)} \quad (5)$$

- Recuperator

$$P_{rec} = \dot{m} \cdot (h_5 - h_2) \quad (6)$$

$$\eta_{rec} = \frac{T_5 - T_2}{T_4 - T_2} \quad (7)$$

- Turbine

$$P_t = \dot{m} \cdot (h_3 - h_4) \quad (8)$$

$$\eta_t = \frac{(h_3 - h_4)}{(h_3 - h_{4\mathrm{is}})} \quad (9)$$

where P_{cm} is the total compressor power, P_c is the power absorbed by the compressor, net of the mechanical efficiency η_{mec}, h is the specific air flow enthalpy, h_{is} is the isentropic air flow enthalpy, η_{cm} and η_t are the compressor and the turbine isentropic efficiencies respectively, η_{rec} is the recuperator effectiveness and P_{rec} is the recuperator power.

2.5. High Speed Generator and Electronic Power Conversion System (EPCS) Modelling

The High-Speed Generator (HSG) is a Permanent Magnet (PM) synchronous machine that is connected to the electrical grid (400 V–50 Hz 3p) through a bi-directional Electronic Power Conversion System (EPCS), not represented in Figure 1. Such EPCS is composed of a motor drive, for motoring operation (MOTOR mode), and a cascade of Rectifier (REC) and grid connected Inverter (INV) for electricity generation (GENERATOR mode). The model represents only the GENERATOR mode, including the EPCS, in the hypothesis of stationary operation [40]. Indeed, it must be pointed out that since the system's dynamics are mainly governed by thermal and mechanical phenomena, the inclusion of electrical dynamics of the HSG and EPCS was judged not necessary.

The investigated system is therefore composed of the HSG feeding a cascade of passive Rectifier and a commercial regenerative Electronic Load used as active Inverter, as represented in Figure 7. Simplified formulas taken from [41] were used for the converters. For constructive reasons, such Electronic Load uses only two phases over three, and this fact was taken into account in the Inverter model.

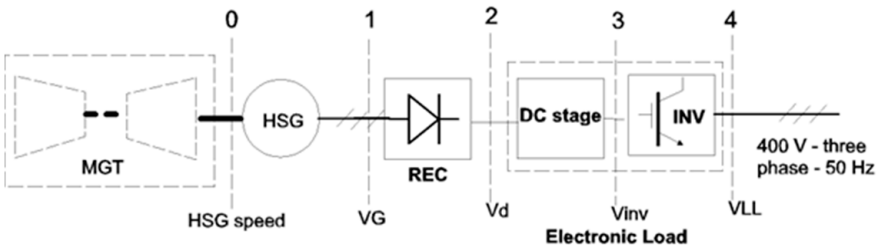

Figure 7. Basic scheme for High-Speed Generator (HSG) connection in generation mode.

The machine-side Rectifier is passive (Diode Rectifier). Therefore, its voltage output is directly connected to the HSG voltage; in turn, such voltage is proportional to the HSG speed, apart from voltage losses.

The "internal" electric scheme of the Electronic Load is not known; it was therefore assumed that the Electronic Load would be composed of an electronic "DC stage" able to match the DC voltage (with a step-up or step-down characteristic) and a PWM Inverter. The parameters were calculated to correspond with the five sections indicated in Figure 7 (0 to 4). More precisely, Section 3 is internal to the Electronic Load and was not actually considered in the calculation.

The model is based on a phasor approach (in the complex plane), with reference to the sections represented in Figure 7. The following notations were used, given a generic parameter X (voltage or current): X is the magnitude of X and $\dot{X}$ is the phasor notation of X. E refers to phase to neutral voltages, while V to phase to phase voltages ($V = \sqrt{3}E$).

The equations considered for each subcomponent are listed below.

$$\text{HSG } \vec{E}0 = \vec{E}1 + RG \cdot \vec{I}1 + j \cdot Xd \cdot \vec{I}1 \tag{10}$$

where $\vec{E}0$ is the "magnet wheel" or no-load voltage, proportional to the HSG speed, $\vec{E}1$ is the output voltage, $\vec{I}1$ is the stator current, RG the phase stator resistance (dependent on temperature, assumed here as 80 °C), Xd the synchronous phase reactance (linearly dependent on frequency), j is the imaginary unit (correspondent to a clockwise 90° rotation in the complex plane). The generic phasor representation is reported in Figure 8.

$$\text{REC } V2 = 1.35 \cdot V1 - \sqrt{3} \cdot R_{Req} \cdot I1 \tag{11}$$

where $V2$ is the DC output voltage and R_{Req} is the "equivalent" resistance of the Rectifier, such that $3 \cdot R_{Req} \cdot I1^2$ corresponds to the Rectifier losses. The "DC stage" adapts its output in order that the DC input to the "Inverter stage" is sufficient to inject power to the grid, independently of the DC input to the Electronic Load. It was therefore assumed for simplicity as a loss-less DC transformer. Indeed, all losses of the Electronic Load are associated to the "Inverter stage". The Inverter was assumed to be a P WM (Pulse Width Modulated wave) type, able to produce a controllable output Power Factor and Voltage. The output voltage is:

$$\text{INV } V4 = ma \cdot 0.612 \cdot V3 - \sqrt{3} \cdot R_{I_{eq}} \cdot I4 \tag{12}$$

where ma is the modulation factor, RI_{eq} is the "equivalent" resistance of the Electronic Load, such that that $2 \cdot RI_{eq} \cdot I4^2$ corresponds to the Electronic Load losses. The following power relations were applied thoroughly:

$$\text{Active Power } P = \sqrt{3} \cdot V \cdot I \cdot \cos(\varnothing) \tag{13}$$

$$\text{Reactive electric power } Q = \sqrt{3} \cdot V \cdot I \cdot \sin(\varnothing) \tag{14}$$

$$\text{Apparent electric power } N = \sqrt{3} \cdot V \cdot I \tag{15}$$

$$P0 = P1 + 3 \cdot RG * I1^2 + Add\_Losses \tag{16}$$

where $P0$ is the mechanical Power transmitted by the MGT to drive the HSG generator, $P1$ is the active power produced by the HSG, $3 \cdot RG \cdot I1^2$ accounts for the ohmic losses in the stator, Add_Losses represent the additional losses. They were assumed proportional to the speed in the assumed speed range:

$$Add\_Losses = K_{add} \cdot n \tag{17}$$

where n is the generator speed and K_{add} is a constant determined in such a way that, at nominal speed and nominal current, the sum of ohmic losses and additional losses be equal to nominal losses calculated from the nominal generator efficiency. Mechanical losses were assumed equal to zero since they comprise the MGT bearing/friction losses:

$$P1 = P2 + 3 \cdot R_{Re_q} \cdot I1^2 \tag{18}$$

where $3 \cdot R_{Req} \cdot I1^2$ accounts for the Rectifier losses, as mentioned above.

$$P4 = P2 - Elec\_Load\_losses \tag{19}$$

where *Elec_Load_losses* are the losses in the Electronic Load. In absence of detailed information, it was assumed that $\frac{1}{4}$ of such losses is "fixed" and $\frac{3}{4}$ of them are proportional to the squared current (ohmic losses).

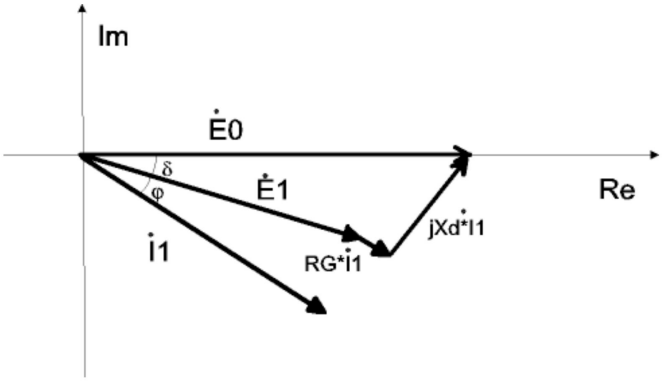

Figure 8. HSG generators phasors.

Simulation Results

The stationary behaviour was investigated varying the stator current (*I*1) in the range 1–15 A, and the generator speed from 100 to 150 krpm. The current value was increased up to 15 A even if the nominal current was 13 A, to account for possible overloading in short periods (transients). The grid voltage was assumed as the nominal value of 400 V; the results (mostly in terms of currents, less in terms of power flows and efficiencies) can vary if the grid voltage is lower or higher (+/−10%). Power Factor (*PF*) of injection to the grid was also assumed equal to 1; also, in this case the results can be different if such *PF* is lower.

The power to the grid, as a function of the Generator Current IG varying the MGT speed from 100 to 150 krpm, is shown in Figure 9a. As shown in the Figure, the power increase tends to "saturate" at high currents, due to the increasing voltage drops associated with higher currents.

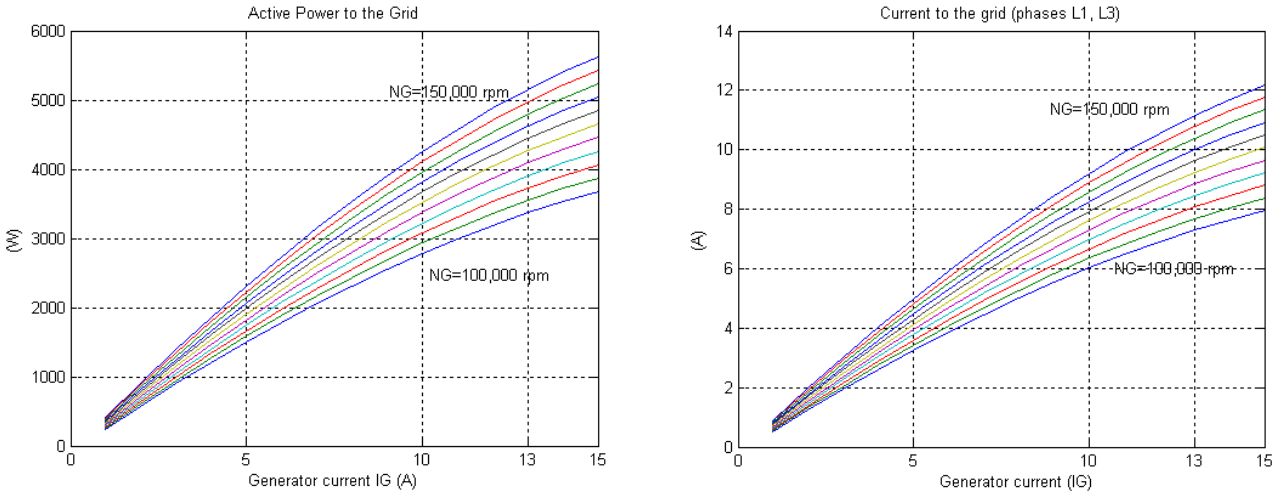

(**a**) (**b**)

Figure 9. (**a**) Calculated power to the grid as a function of the Generator Current IG varying the MGT speed from 100 to 150 krpm; (**b**) Calculated current injected to the grid a function of the Generator Current IG varying the MGT speed from 100 to 150 krpm.

Even at 150 krpm and 15 A, the HSG power output to the grid is limited at 5.625 W. The grid current is shown in Figure 9b and it can be seen that its behaviour is similar to the power pattern. Maximum current injected to the grid is in the order of 12 A in

correspondence of 150 krpm and 15 A of generator current. It must be noted that the Electronic Load operates with only 2 phases over 3.

The HSG active power is shown in Figure 10a, its behaviour is similar to the power to the grid graph. The maximum power value is 6060 W in correspondence of 15 A and 150 krpm; since the HSG is assumed to operate with a PF = 0.955, correspondent to the passive Rectifier load, the machine produces a limited amount of reactive power, represented in Figure 10b, whose maximum is in the order of 1900 VAR (roughly 1500 VAR in nominal conditions).

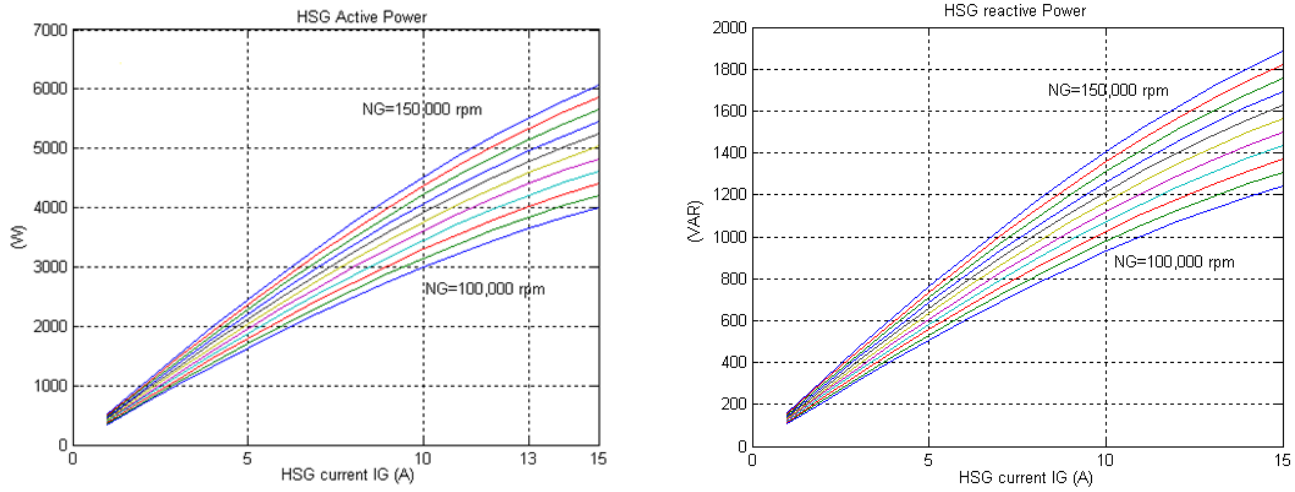

(**a**) (**b**)

Figure 10. (**a**) Calculated HSG Active Power as a function of the HSG current IG varying the MGT speed from 100 to 150 krpm; (**b**) Calculated HSG reactive Power as a function of the HSG current IG varying the MGT speed from 100 to 150 krpm.

In Figure 11a, the HSG mechanical power loading at the MGT axis shows that the maximum absorbed Power is 6520 W in correspondence of 150 krpm and 15 A. In Figure 11b, the resulting mechanical torque has a maximum of roughly 0.41 Nm calculated at 15 A of stator current IG.

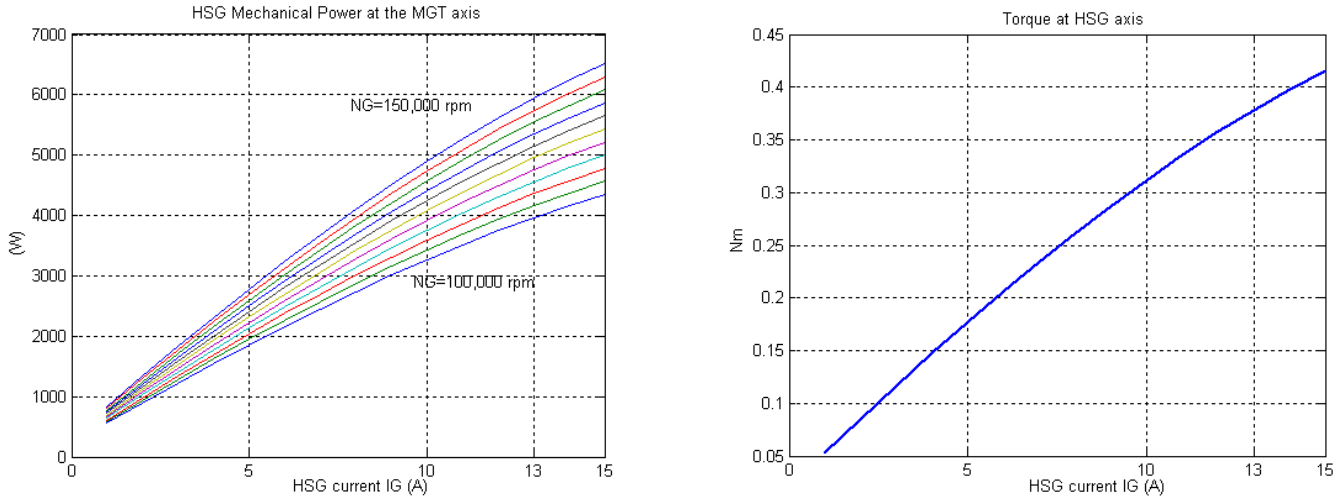

(**a**) (**b**)

Figure 11. (**a**) Calculated HSG mechanical Power at MGT shaft as a function of the generator current IG, varying the MGT speed from 100 to 150 krpm; (**b**) Calculated HSG Torque at MGT shaft as a function of the generator current IG varying the MGT speed from 100 to 150 krpm.

The torque is practically independent from speed, and depends only on stator current IG, since no mechanical losses were assumed.

In Figure 12a, the mechanical Power (P0), the active Power (P1) in the HSG, the rectified Power input to the Electronic Load (P2) and the Power injected to the grid (P4) at the two min/max speed levels, 100–150 krpm, are represented, respectively. Most of the losses are associated to the HSG (ohmic and additional) and to the Electronic Load.

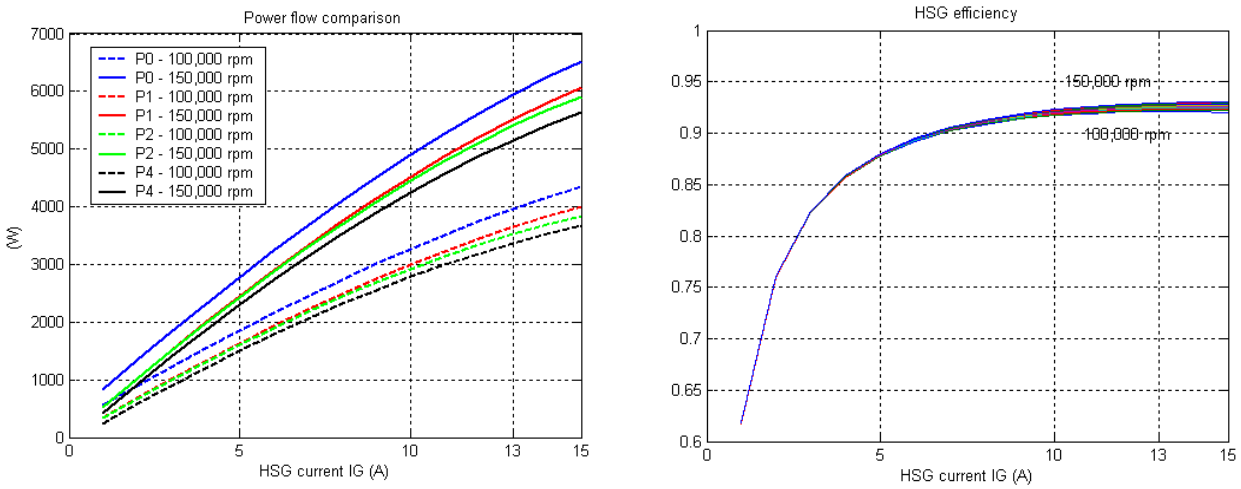

(**a**) (**b**)

Figure 12. (**a**) Comparison of Power flows (mechanical Power (P0), active Power (P1), rectified Power input to the Electronic Load (P2), and Power injected to the grid (P4)) as a function of generator current IG at different speed levels; (**b**) HSG calculated efficiency as a function of the generator current IG varying the MGT speed from 100 to 150 krpm.

The HSG efficiency Figure 12b is mostly influenced by the load (current) and only in a limited way by the speed, since no mechanical losses were assumed. Values at full load range are in the range of 92–93% and drop to 60% at very low load.

The total efficiency (from HSG axis to electric power to the grid) is represented in Figure 13a. The maximum values range from 0.85 to 0.87, depending on speed. The efficiency remains higher than 80% until 1/3 of the load, while it drops to 50% at very low loads.

Finally, Figure 13b the total efficiency is represented as a function of the net electric output P4 at three speed levels: minimum speed (100 krpm), close to nominal speed (125 krpm) and maximum speed (150 krpm). The speed regulation has to be managed in order to maximize such efficiency, considering at the same time the MGT efficiency.

The modelling allowed us to determine that the HSG/EPCS assembly is able to generate about 5 kW_e; maximum levels of 5.6 kW could be achieved "overcharging" the HSG up to 15 A and operating the MGT at the very high-speed level of 150 krpm. Such operation conditions could presumably be compatible with the system for very short transients. Nominal service (13 A, 130 krpm) will limit output power to the grid to approximately 4.5 kW.

The efficiency of the HSG appears to be higher than 80% from 1/3 of the load to full load.

The results of the HSG stationary simulation were entered into the system model in the form of performance maps, where the HSG electrical efficiency η_{ele} depends on the mechanical power available at the shaft ($P0 = P_t - P_{cm}$) and the generator speed n. From these parameters, applying the Equation (20), it was possible to calculate the system electrical power output P_{ele}.

$$P_{ele} = (P_t - P_{cm}) \cdot \eta_{ele} \quad (20)$$

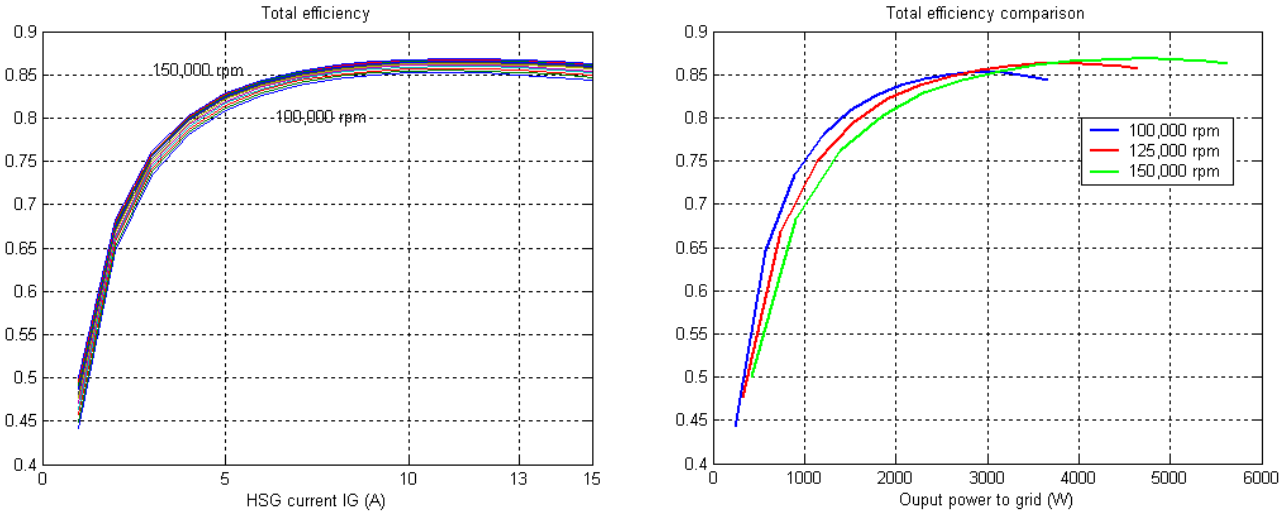

(**a**) (**b**)

Figure 13. (**a**) Total efficiency (net grid electric power/input mechanical power) as a function of the generator current IG varying the MGT speed from 100 to 150 krpm; (**b**) Total calculated efficiency as a function of net grid output Power P4 varying the MGT speed from 100 to 150 krpm.

3. Results and Discussion

The system model resulting from the integration of the components previously described (dish, receiver, MGT, HSG) was applied to guide the design of the demo plant, both in terms of components and control strategy definition, and to predict the performance of the demo plant on a yearly basis with the aim of providing useful data for the technology optimisation.

In the following, the procedure adopted for the system model application is described.

As a first step, assuming a constant ambient temperature of 15 °C, the integrated model was used to describe the system performance (output power, efficiencies, etc.) varying two independent parameters (DNI, generator speed, TIT (Turbine Inlet Temperature), etc.). Indeed, the implemented model, in the absence of a control strategy, has two degrees of freedom. Therefore, a set of possible operation curves was generated, as represented in Figure 14.

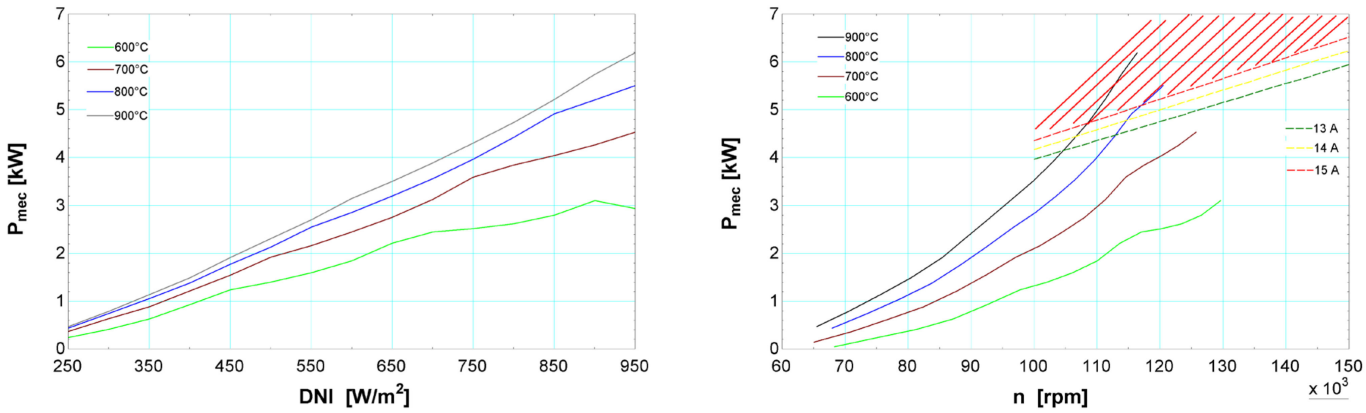

(**a**) (**b**)

Figure 14. Example of parametric analysis: (**a**) mechanical power produced at different DNI varying the TIT; (**b**) mechanical power available at the shaft at different MGT speed rates varying the TIT.

Successively, a unique operating line was selected to optimise the system performance. The definition of a unique operating curve, which univocally correlates the system operation to the DNI value, depends on the operation strategy adopted. In the framework of the project, it was agreed to make the system work under the following conditions:

- For stator current lower than 13 A, the TIT is kept constant at the design value of 800 °C for maximizing the cycle efficiency and therefore the electrical power output. This can be achieved acting on the generator load to regulate the MGT speed and consequently the mass flowrate. The resulting operating line is represented, as an example, by the blue curves in Figure 14a,b;
- After reaching the value of 13 A, the stator current is kept constant acting on the load, obtaining an increase of the MGT speed and therefore a reduction of the TIT. The operating line can be represented by the dotted green line in Figure 14b;
- Once the maximum allowable speed is reached (150 krpm), the defocusing action must be applied.

Therefore, for every DNI value a unique MGT speed level exists that satisfies the conditions mentioned above, as represented in Figure 15, where the MGT speed is represented as a function of DNI, along with the mechanical power available at the shaft and the electrical power output. In the same figure, the performance of the system considering an improved electrical generator, not subjected to the limitation of the stator current at 13 A, is represented. Indeed, as mentioned in the previous paragraph, this current limitation leads to a restraint in the mechanical load on the MGT shaft, which can reach a maximum value of 6.5 kW in short transients, while a safer level is in the order of 5.2 kW, corresponding to an electrical power output of about 4.5 kW_e. By an upgrade of the electrical generator, even keeping unchanged the performance of the other components (dish, receiver, MGT), the electrical power output in the design conditions (800 °C) would see an increase of 0.3 kW_e, from 4.2 kW_e to 4.5 kW_e, as represented in Figure 15.

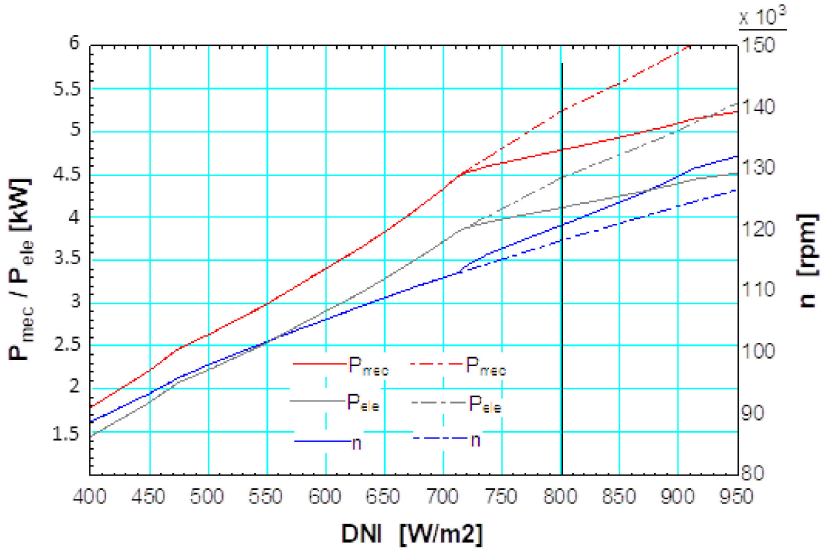

Figure 15. System performance (mechanical power available at the shaft, electrical power output, generator speed) as a function of DNI. The continuous and the dotted lines are referred to the present and the "generator optimised" systems, respectively.

The procedure mentioned above was replicated for different ambient temperature values to build the off-design performance tables, which univocally correlate the system parameters (temperatures, pressures, mass flow rate, power produced, efficiencies) to the meteorological data (DNI and ambient temperature).

These tables are typically used in the simulation of solar power plants to perform system analysis for any given combination of DNI and ambient temperature, reducing

the computational burden. Indeed, the transient system simulation, which would require the calculation of a self-consistent set of variables at each time step, becomes a trivial interpolation of data. In the present work these matrices were applied to run transient simulations of the demo plant, considering the yearly meteorological data registered in the Casaccia site as the time-dependent input.

In the present work four system matrices were built, referred to with the following demo configurations: system with volumetric receiver option, system with volumetric receiver option and optimised generator, system with cavity receiver option, and system with cavity receiver option and optimised generator. These matrices were applied to run transient simulations of the demo plant, considering the yearly meteorological data registered in the Casaccia site as the time-dependent input. In Figure 16, the visual representation of the off-design matrix for the cavity receiver option is shown, reporting the following system parameters: *TIT*, *Pressure ratio*, $\dot{m}$, n, net mechanical power available at the shaft, net electrical power output, electrical efficiency (ratio of the electricity produced to the mechanical power available at the shaft) and cycle efficiency (ratio of the electrical power output to the net power absorbed by the receiver).

As mentioned in the previous paragraphs, the system model was also used to guide the revision of the receiver design, with the aim of increasing the power input to the system to compensate for the unexpected and limited performance of the dish. A window diameter of 22 cm was selected for both the cavity and volumetric receivers, to increase the demo power output and to provide a wider range of operation for the MGT. A further increase of the receiver window diameter was not a viable solution to raise the system power output due to the limitations in the concentration ratio and consequently the maximum temperature achievable in the receiver.

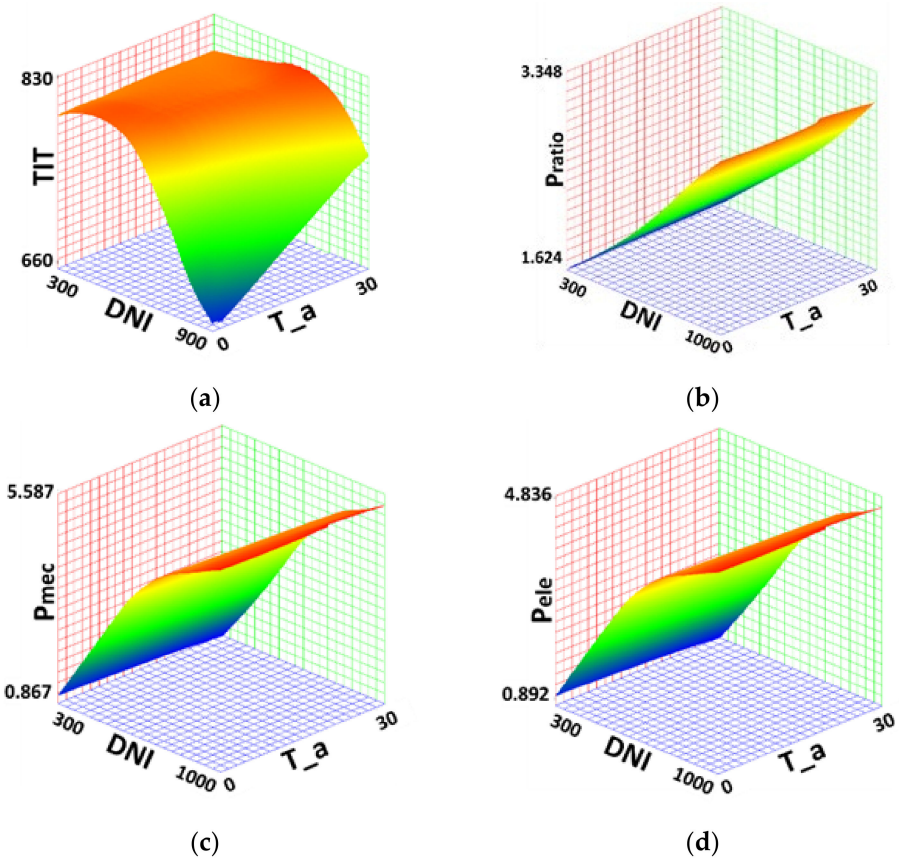

Figure 16. *Cont.*

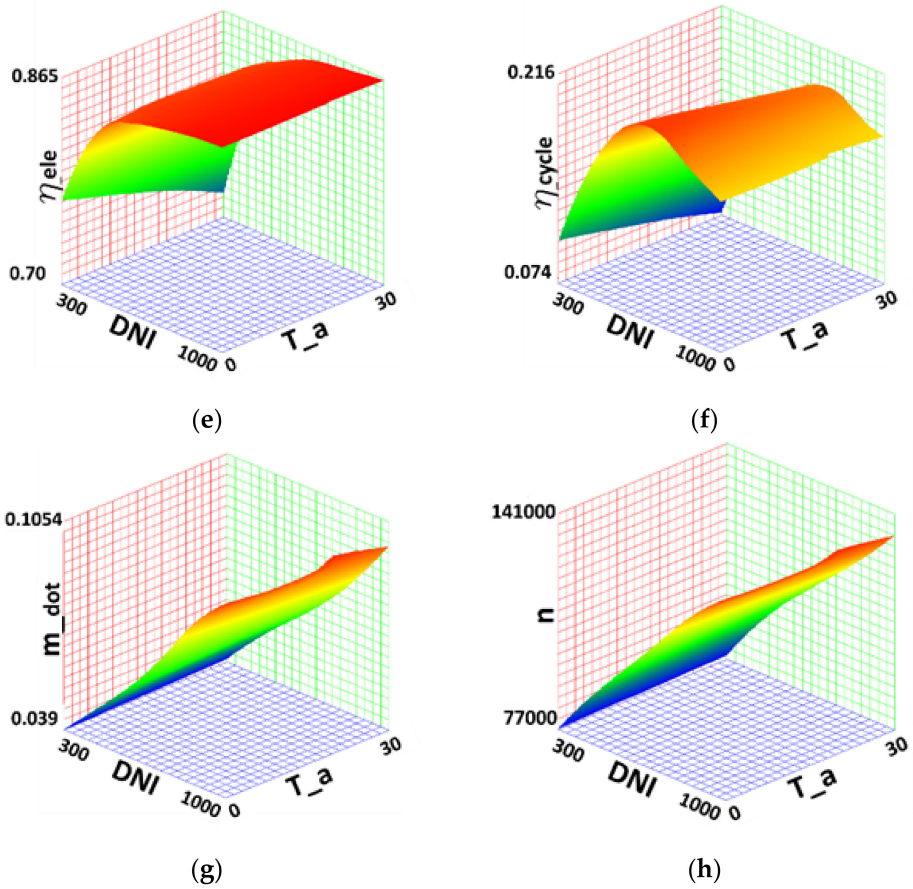

Figure 16. System performance for any given combination of DNI and Ta (cavity receiver option, receiver window diameter: 22 cm). (**a**) TIT (°C); (**b**) Compressor Pratio; (**c**) Mechanical power available at the shaft (kW); (**d**) Electrical power output (kW_e); (**e**) Electrical efficiency; (**f**) Cycle efficiency; (**g**); $\dot{m}$ (kg/s); (**h**) n (rpm).

Demo Plant Simulation on a Yearly Basis

In Figure 17, the yearly average DNI time-series measured in the Casaccia site over the period 2006–2015, calculated on the base of a statistical approach [28], is represented, starting from the first of January until the end of December, with a sampling rate of 1 h. These experimental data, together with the ambient temperature data, were used for the transient simulation of the demo system, whose results are represented in Figure 18 and synthesized in Table 3.

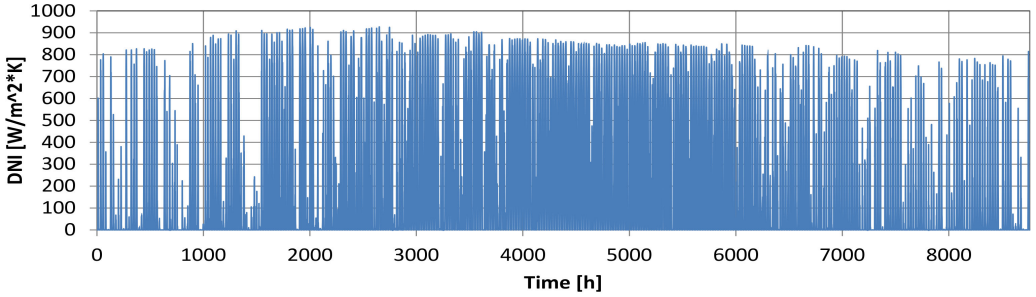

Figure 17. Annual DNI time-series measured at ENEA Casaccia site.

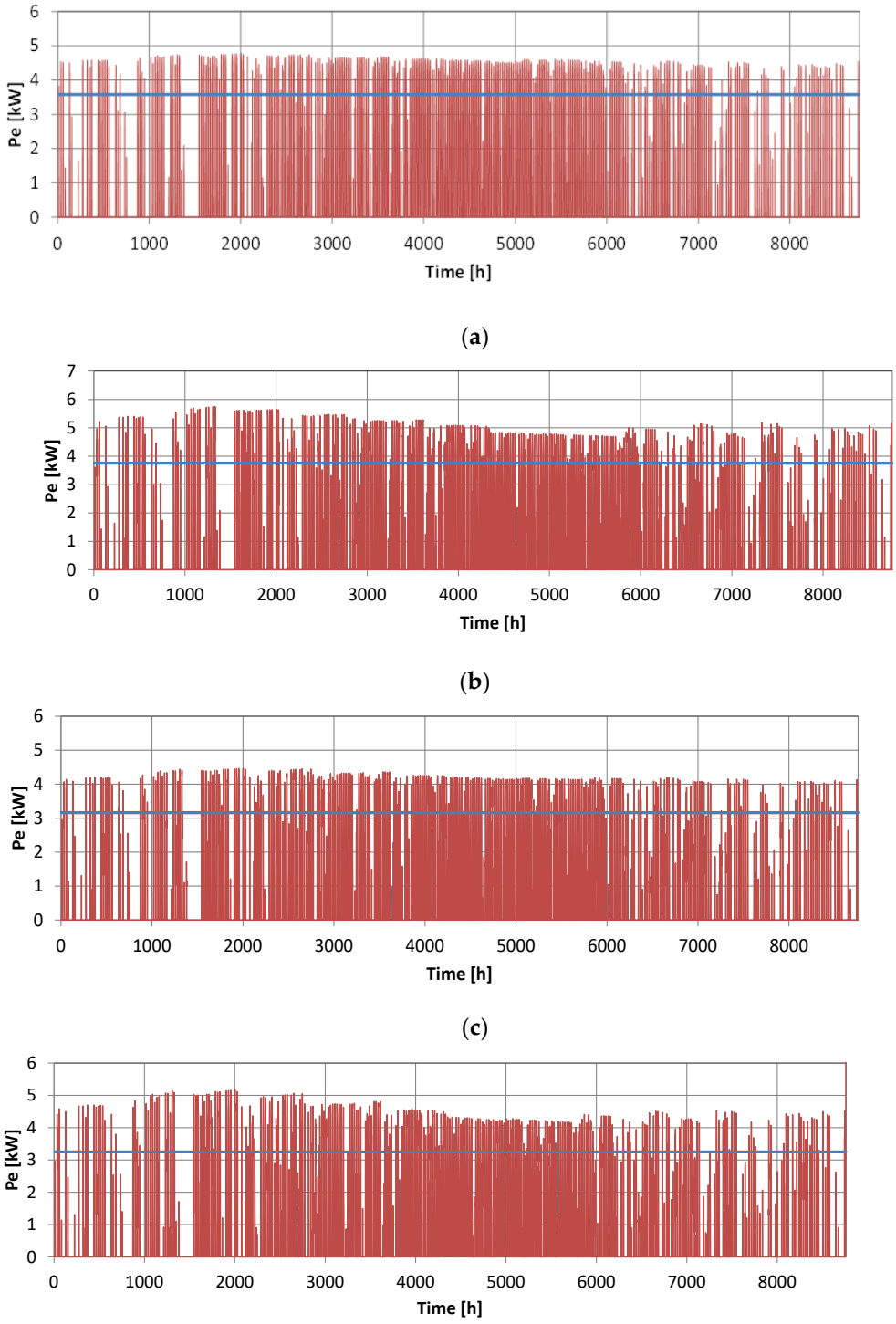

Figure 18. Time-series of the electrical power produced and annual average value. (**a**) volumetric receiver option; (**b**) volumetric receiver option with optimised generator; (**c**) cavity receiver option; (**d**) cavity receiver option with optimised generator.

Table 3. Annual average system parameters for the Casaccia site. System configuration: (**a**) volumetric receiver option; (**b**) volumetric receiver option with optimised generator; (**c**) cavity receiver option; (**d**) cavity receiver option with optimised generator.

	System Configuration			
	a	**b**	**c**	**d**
Operating hours	2374	2374	2374	2374
Capacity Factor	0.21	0.22	0.19	0.19
Electrical power output [kW_e]	3.58	3.75	3.16	3.25
Mechanical power available at the shaft [kW]	4.17	4.40	3.70	3.82
TIT [°C]	780	800	786	800
Mass flow rate [kg/s]	0.076	0.074	0.067	0.066
Receiver efficiency	0.812	0.811	0.700	0.700
Compressor efficiency	0.717	0.718	0.710	0.711
Turbine efficiency	0.809	0.809	0.800	0.800
Generator efficiency	0.849	0.847	0.843	0.841
Cycle efficiency	0.170	0.177	0.173	0.177
Global efficiency	0.059	0.062	0.052	0.053

In particular, Figure 18 represents the electrical power output for the four scenarios considered: system with volumetric receiver option, system with volumetric receiver option and optimised generator, system with cavity receiver option, and system with cavity receiver option and optimised generator. Obviously, the best performance, in terms of electricity produced, is achieved in the case of the volumetric receiver option (average output power: 3.58 kW) since the cavity configuration (average output power: 3.16 kW) is penalized by the lower thermal efficiency of the solar receiver itself. The improvement of the sole generator does not seem to significantly an increase in the system performance on the annual basis (3.75 kW vs. 3.58 kW in the case of volumetric receiver configuration, and 3.25 kW vs. 3.16 kW in the case of cavity receiver system). Differently, the optimisation of the solar dish, with the upgrade of the other system components, would even double the design system power output (~10 kW_e), considering that the present overall optical efficiency is around 40% and that a realistic value is about 80%. To synthesize the system simulation result, in Table 3 the main parameters, yearly averaged, are reported. Regarding the cycle efficiency, the averaged value is quite homogeneous, about 0.17, whereas the target value is 0.21. In a theoretical analysis conducted by Semprini et al. [24], an optimised solar dish-MGT system of the same configuration (simple recuperated Brayton cycle) and size as the OMSoP pilot (6.9 kW_e vs. 5 kW_e), and with quite close design specifications (TIT: 800 °C, $\dot{m}$: 88 g/s) but highest pressure ratio (3.65 vs. 2.9), had a calculated cycle efficiency equal to 0.23.

The average capacity factor for the Casaccia site (Rome) ranges from 0.19 (scenarios *c* and *d*) to 0.22 (scenario *b*). These values are in line with the results presented by other authors for the same technology, considering that the capacity factors calculated for the OMSoP system in moderate irradiated countries is 0.21 [42], whereas for very favourable locations (such as South Africa and Morocco) it could be higher than 35% [42]. In this regard it is worth noting that the Casaccia site is characterized by a quite heterogeneous solar irradiation along the year, which, in the absence of thermal storage significantly penalizes the annual capacity factor (i.e., in July the average daily irradiation is 7.81 kWh/m^2 whereas in January the average daily irradiation is 2.84 kWh/m^2 [43].

Regarding the system global efficiency, intended as the ratio of the power output to the solar power collected by the dish, in the case of the volumetric option the annual mean value is 0.059, while for the cavity configuration it is 0.052. This parameter is significantly affected by the abovementioned oversizing of the dish and its poor optical performance (40% in place of the expected 80%). In a realistic perspective the average global efficiency should be about 0.12 while, taking into account some feasible design improvements on the other components, it could be raised up to 0.18 (with dish optical efficiency: 0.8;

receiver efficiency: 0.8; TIT: 900 °C; generator efficiency: 0.9; compressor pressure ration: 3.6). Indeed, as evaluated by Gavagnin et al. [44], considering an increase of 100 °C in the TIT, and therefore the solar receiver operating at 900 °C in place of 800 °C, the cycle efficiency in design condition can raise up to 31% and the global efficiency up to 19.8%. To clarify the validity of these performance figures it is worth noting that in other theoretical analyses published in the field of hybrid solar dish-MGT systems, the assumptions on the components design specifications are more optimistic, for example, in different studies the dish optical efficiency is assumed equal to 0.9 [25].

4. Conclusions and Future Work

A demonstration plant that integrates the solar dish and the MGT technologies for renewable electricity production was developed within the European-funded OMSoP project and was installed at the ENEA Casaccia site.

A transient system model, capable of predicting the plant behaviour at different meteorological conditions (DNI and ambient temperature) was developed by ENEA. This activity has required an iterative approach, with a gradual refinement of the component models on the base of the available updates on system design, specifications and testing.

The resulting model was applied for different purposes: to define the optimal system parameters, to help the elaboration of an operational strategy to maximize the overall plant efficiency, and to guide the improvement of the single components. As an example from the simulation of the HSG component, it clearly emerged that the system, as realized for the demonstrative activity, is able to generate, in nominal conditions, 4.5 kW in place of the expected 5 kW due to the limitation of the stator current to 13 A, while maximum levels of 5.6 kW could be achieved "overcharging" the HSG up to 15 A and operating the MGT at the very high speed of 150 krpm. Such an operation could presumably be compatible for very short transients.

The system model was also applied to predict the performance of the demo plant installed at the ENEA Casaccia site on a yearly basis, with the aim of providing useful data for a design revision.

To this purpose, the operation matrices for the calculation of the demo system behaviour in off-design conditions were built, considering four plant configurations: (a) system with volumetric receiver option, (b) system with volumetric receiver option and optimised generator, (c) system with cavity receiver option, and (d) system with cavity receiver option and optimised generator. The yearly average statistical DNI time-series measured in the Casaccia site over the period 2006–2015 was used as time-dependent input. From the transient simulation of the demo system, it clearly emerged that the best performance, in terms of electricity production, is achieved with the volumetric receiver option (average output power: 3.58 kW) since the cavity configuration is penalized by the lower thermal efficiency of the solar receiver itself. Regarding the TIT, its average value on a yearly basis ranges from 780 to 800 °C, whereas the nominal TIT is 800 °C. Regarding the cycle efficiency, the averaged value is quite homogeneous, about 0.17, whereas the nominal value is 0.21. Regarding the system global efficiency, intended as the ratio of the power output to the solar power collected by the dish, in the case of the volumetric option the annual mean value is 0.059, while for the cavity configuration it is 0.052. This parameter is significantly affected by the oversizing of the pilot dish compared to the size of the MGT. In a realistic perspective, the average global efficiency should be about 0.12 while, taking into account some feasible design improvements on the other components, it could be raised up to 0.18 (with dish optical efficiency: 0.8; receiver efficiency: 0.8; TIT: 900 °C; generator efficiency: 0.9; compressor pressure ratio: 3.6). Indeed, by considering an increase of 100 °C in the TIT and therefore the solar receiver operating at 900 °C in place of 800 °C, the cycle efficiency in design condition would increase up to 31% and the global efficiency up to 19.8%. The present capacity factor ranges from 0.19 (scenarios *c* and *d*) to 0.22 (scenario *b*) but, considering a more favourable geographical scenario (South Africa, Morocco), the capacity factor could be higher than 35%.

The improvement of the sole generator does not seem to significantly increase the power output on the annual basis (3.75 kW vs. 3.58 kW). Differently, the optimisation of the solar dish, with the upgrade of the other system components, would even double the system power output (~10 kW_e), considering that the present overall optical efficiency is around 40% and that a realistic value can be about 80%.

These results represent a fair approximation of the demo system behaviour, but more detailed component models will be developed in the future to provide a realistic description of the dynamics of the system in transient operation mode (start-up, shut down, irradiance fluctuations). Particularly, the thermal inertia of the cavity receiver installed in the OMSoP facility will be integrated in the system and described by empirical correlations derived from the experimental data. This will help in individuating possible criticalities in the heating phase, such as temperature ramps too fast and/or local over-heating in the hot components (receiver, turbine, shaft). Furthermore, this will allow identification of the frequency and the duration of system transient operations, and consequently possible wear issues on the components.

Additionally, as a further step of the development of this innovative technology, the integration of a thermal storage unit capable of smoothing the system transient operation and stabilizing the electricity production in the presence of irradiance fluctuations will be investigated. To this end, the abovementioned dynamic system model will be applied to simulate the performance of an upgraded dish-MGT configuration, equipped with a thermal energy storage unit and characterized by a high degree of flexibility and dispatchability, in order to individuate the most promising thermal storage option (material, size, design) and assess its technical feasibility.

Author Contributions: Conceptualization, M.L. and J.A.-Z.; methodology, M.M., M.F. and L.A.; software, V.R., M.L.; validation, J.A.-Z. and L.A.; formal analysis, M.M. and M.F.; investigation, M.L., V.R. and J.A.-Z.; resources, M.L. and J.A.-Z.; data curation, V.R.; writing—original draft, M.L., M.F., J.A.-Z. and M.M. All authors have read and agreed to the published version of the manuscript.

Funding: This research was supported by the European Commission through the Seventh Framework Programme (FP7), project OMSoP, Grant agreement No.: 308952.

Data Availability Statement: The data used in the research are based on demonstration activities of OMSoP (Optimised Microturbine Solar Power system) project. The details of the designs, characterisation of the system and testing setup and procedures are available on the project website at: https://etn.global/research-innovation/projects/omsop and https://cordis.europa.eu/project/id/308952/reporting (accessed on 17 December 2021).

Acknowledgments: The authors wish to thank Bjorn Laumert for technical information on the solar receivers developed within the project, Mohsen Ghavami, Mahmoud Khader and Abdulnaser Sayma for technical information and guidance on the MGT components, and Anders Malmquist and Lars Malrup for their experience and support on the MGT control logic.

Conflicts of Interest: The authors declare no conflict of interest.

Nomenclature

Abbreviations

CF	Concentration Factor
CSP	Concentrating Solar Power
CFD	Computational Fluid Dynamics
DC	Direct Current
DNI	Direct Normal Irradiance
EES	Engineering Equation Solver
EL	Electroni Load
EPCS	Electron. Power Conv. System
FEA	Finite Elements Analysis
HSG	High Speed Generator
INV	Inverter

MGT	Micro Gas Turbine
PM	Permanent Magnet
PWM	Pulse width Modulated Wave
REC	Rectifier
SCR	Sun-radiation Conic Reflectance
TIT	Turbine Inlet Temperature
PF	Power factor
Symbols	
ΔP	Pressure drops [Pa]
*E*0	No load voltage [V]
*E*1	Output voltage [V]
h	Specific air enthalpy [kJ/kg]
I	Current [A]
*I*1	Stator Current [A]
j	Imaginary unit
Kadd	Electric constant [W/rpm]
$\dot{m}$	Air mass flow rate [kg/s]
ma	Modulation factor
n	MGT speed [rpm]
N	Apparent elec. power [VA]
P	Power [W]
Pratio	Compressore Pressure ratio
PR	Pratio, net of Press. drops
*P*0	HSG Mechanical power
*P*1	HSG Active power
*P*2	Rectified Power to the EL
*P*4	Power to the grid
RG	Phase Stator Resistance
T	Temperature [K]
V	Voltage [V]
RReq	REC Resistance [Ω]
RIeq	EL Resistance [Ω]
Q	Reactive El. Power [VAR]
Xd	Syn. phase reactance [Ω]
H	Efficiency [-]
Subscripts	
c, *c m*	compressor
ele	electrical
Is	isoenthropic
mec	mechanical
R	receiver
rec	recuperator
T	turbine
W	window

References

1. International Energy Agency. *Harnessing Variable Renewables: A Guide to the Balancing Challenge*; OECD/IEA: Paris, France, 2011.
2. Sánchez, D.; Frej, H.; Muñoz de Escalona, J.M.; Chacartegui, R.; Sánchez, T. Alternative Approach to Determining the Preferred Plant Size of Parabolic trough CSP Power Plants—GT2011-46585. In Proceedings of the ASME Turbo Expo 2011, Vancouver, BC, Canada, 6–10 June 2011; pp. 1053–1062.
3. ARENA. Comparison of Dispatchable Renewable Electricity Options, Technologies for an Orderly Transition. 2018. Available online: https://www.solarpaces.org/wp-content/uploads/Comparison-of-Dispatchable-Renewable-Energy-Options-Technologies-for-an-Orderly-Transition.pdf (accessed on 17 December 2021).
4. Sanchez, D.; Bortkiewicz, A.; Rodríguez, J.M.; Martínez, G.S.; Gavagnin, G.; Sánchez, T. A methodology to identify potential markets for small-scale solar thermal power generators. *Appl. Energy* **2016**, *169*, 287–300. [CrossRef]
5. Ahmadi, M.H.; Ahmadi, M.A.; Mellit, A.; Pourfayaz, F.; Feidt, M. Thermodynamic analysis and multi objective optimization of performance of solar dish Stirling engine by the centrality of entransy and entropy generation. *Int. J. Electr. Power Energy Syst.* **2016**, *78*, 88–95. [CrossRef]

6. Barreto, G.; Canhoto, P. Modelling of a Stirling engine with parabolic dish for thermal to electric conversion of solar energy. *Energy Convers.Manag.* **2017**, *132*, 119–135. [CrossRef]
7. Guarino, S.; Catrini, P.; Buscemi, A.; Lo Brano, V.; Piacentino, A. Assessing the Energy-Saving Potential of a Dish-Stirling Concentrator Integrated into Energy Plants in the Tertiary Sector. *Energies* **2021**, *14*, 1163. [CrossRef]
8. Mancini, T.; Heller, P.; Butler, B.; Osborn, B.; Schiel, W.; Goldberg, V.; Buck, R.; Diver, R.; Andraka, C.; Moreno, J. Dish-Stirling Systems: An Overview of Development and Status. *J. Sol. Energy Eng.* **2003**, *125*, 135–151. [CrossRef]
9. Laria, D.; Al Zaili, J.; Sayma, A. Solar Dish Micro Gas Turbine Technology for Distributed Power Generation. In *Sustainable Energy Technology and Policies*; Springer: Singapore, 2017.
10. Optimised Microturbine Solar Power System OMSoP. Available online: https://etn.global/research-innovation/projects/omsop/ (accessed on 17 December 2021).
11. Lanchi, M.; Montecchi, M.; Crescenzi, T.; Mele, D.; Miliozzi, A.; Russo, V.; Mazzei, D.; Misceo, M.; Falchetta, M.; Mancini, R. Investigation into the coupling of micro gas turbines with CSP technology: OMSoP project. *Energy Procedia* **2015**, *69*, 1317–1326. [CrossRef]
12. Wang, W.; Ragnolo, G.; Aichmayer, L.; Strand, T.; Laumert, B. Integrated design of a hybrid gas turbine-receiver unit for a solar dish system. *Energy Procedia* **2015**, *69*, 583–592. [CrossRef]
13. Arroyo, A.; McLorn, M.; Fabian, M.; White, M.; Sayma, A. Rotor-Dynamics of Different Shaft configurations for a 6 kW Micro Gas Turbine for Concentrated Solar Power. In Proceedings of the ASME Turbo Expo 2016: Turbomachinery Technical Conference and Exposition, Seoul, Korea, 13–17 June 2016; Volume 8, pp. V008T23A009–V008T23A019.
14. Ahmadi, M.H.; Ahmadi, M.A.; Feidt, M. Performance Optimization of a Solar-Driven Multi-Step Irreversible Brayton Cycle Based on a Multi-Objective Genetic Algorithm. *Oil Gas Sci.Technol.—Rev. d'IFP Energ. Nouv.* **2016**, *71*, 16. [CrossRef]
15. Ahmadi, M.H.; Alhuyi, N.M.; Ghasempour, R.; Pourfayaz, F.; Rahimzadeh, M.; Ming, T. A review on solar-assisted gas turbines. *Energy Sci. Eng.* **2018**, *6*, 658–674. [CrossRef]
16. Schwarzbozl, P.; Buck, R.; Sugarmen, C.; Ring, A.; Crespo, J.M.; Altwegg, P.; Enrile, J. Solar gas turbine systems: Design, cost and perspectives. *Sol. Energy* **2006**, *80*, 1231–1240. [CrossRef]
17. Bellos, E.; Tzivanidis, C.; Antonopoulos, K.A. Parametric analysis and optimization of a solar assisted gas turbine. *Energy Convers. Manag.* **2017**, *139*, 151–165. [CrossRef]
18. Heller, P.; Pfander, M.; Denk, T.; Tellez, F.; Valverde, A.; Fernandez, J.; Ring, A. Test and Evaluation of a Solar Powered Gas Turbine System. *Sol. Energy* **2006**, *80*, 1225–1230. [CrossRef]
19. SOLHYCO Project. Available online: https://cordis.europa.eu/project/id/19830/reporting (accessed on 17 December 2021).
20. Quero, M.; Korzynietz, R.; Ebert, M.; Jiménez, A.A.; Del Río, A.; Brioso, J.A. Solugas—Operation Experience of the First Solar Hybrid Gas Turbine System at MW Scale. *Energy Procedia* **2013**, *49*, 1820–1830. [CrossRef]
21. Pégase Project, CNRS, France. Available online: https://www.cnrs.fr/cw/dossiers/dosolaireE/contenu/alternative/alter2_textes.html (accessed on 17 December 2021).
22. Yang, J.; Xiao, G.; Ghavami, M.; Al-Zaili, J.; Yang, T.; Sayma, A.; Ni, D. Thermodynamic modelling and real-time control strategies of solar micro gas turbine system with thermochemical energy storage. *J. Clean. Prod.* **2021**, *304*, 127010. [CrossRef]
23. Laria, D.; Zhou, X.; Al Zaili, J.; Zhang, Q.; Xiao, G.; Sayma, A. Development of a Model for Performance Analysis of a Honeycomb Thermal Energy Storage for Solar Power Microturbine Applications. *Energies* **2019**, *12*, 3968.
24. Semprini, S.; Sanchez, D.; De Pascale, A. Performance analysis of a micro gas turbine and solar dish integrated system under different solar-only and hybrid operating conditions. *Sol. Energy* **2016**, *132*, 279–293. [CrossRef]
25. García-Ferrero, J.; Heras, I.; Santos, M.J.; Merchán, R.P.; Medina, A.; González, A.; Hernández, A.C. Thermodynamic and cost analysis of a solar dish power plant in Spain hybridized with a micro gas turbine. *Energies* **2020**, *13*, 5178. [CrossRef]
26. Montecchi, M.; Cara, G.; Benedetti, A. VISdish: A new tool for canting and shape-measuring solar-dish facets. *Rev. Sci. Instrum.* **2017**, *88*, 065107. [CrossRef]
27. Aichmayer, L.; Garrido, J.; Wang, W.; Laumert, B. Experimental evaluation of a novel solar receiver for a micro gas-turbine based solar dish system in the KTH high-flux solar simulator. *Energy* **2018**, *159*, 184–195. [CrossRef]
28. Khader, M.A.; Ghavami, M.; Al-Zaili, J.; Sayma, A.I. Heat Transfer Effect on Micro Gas Turbine Performance for Solar Power Applications. *Energies* **2021**, *14*, 6745. [CrossRef]
29. Khader, M. Optimised Radial Turbine Design, Project Deliverable D1.8. Available online: https://etn.global/wp-content/uploads/2019/02/D1.8-Optimised-Radial-Turbine-Design.pdf (accessed on 17 December 2021).
30. Khader, M.; Alzaili, J.; Ghavami, M.; Sayma, A. D1.11 A Report on Further MTG Optimisation. Available online: https://etn.global/research-innovation/projects/omsop/#h2igccpublications-and-reports (accessed on 17 December 2021).
31. Deliverable D1.5—Optimized Dish Design, OMSoP Project. Available online: https://etn.global/wp-content/uploads/2019/02/D1.5-Optimized-dish-design.pdf (accessed on 17 December 2021).
32. Qt Cross-Platform Software. Available online: https://www.qt.io/ (accessed on 17 December 2021).
33. Deliverable D1.6—Report on Solar Dish Performance, OMSoP Project. Available online: https://etn.global/research-innovation/projects/omsop/#h2igcc-publications-and-reports (accessed on 17 December 2021).
34. Montecchi, M. Proposal of a New Parameter for the Comprehensive Qualification of Solar Mirrors for CSP Applications. In Proceedings of the AIP Conference Proceeding of SolarPACES, Abu Dhabi, United Arab Emirates, 11–14 October 2016.

35. Nazemi, S.D.; Boroushaki, M. Design, Analysis and Optimization of a Solar Dish/Stirling. *Syst. Int. J. Renew. Energy Dev.* **2016**, *5*, 33–42. [CrossRef]
36. Stine, W.B.; Harrigan, R.W. *Solar Energy Systems Design: A Computer Based Approach*; Wiley: Hoboken, NJ, USA, 1985.
37. Aichmayer, L.; Spelling, J.; Laumert, B. Preliminary Design and Analysis of a Novel Solar Receiver for a Micro Gas-Turbine based Solar Dish System. *Sol. Energy* **2015**, *114*, 378–396. [CrossRef]
38. Aichmayer, L.; Garrido, J.; Laumert, B. Scaling Effects of a Novel Solar Receiver for a Micro Gas-Turbine based Solar Dish System. *Sol. Energy* **2015**, *162*, 248–264. [CrossRef]
39. Khader, M.A. Development of a Micro Gas Turbine for Concentrated Solar Power Applications. Ph.D. Thesis, City University of London, London, UK, 2017.
40. Ghavami, M.; Alzaili, J.; Sayma, A.I. A comparative study of the control strategies for pure concentrated solar power micro gas turbines. In *Turbo Expo: Power for Land, Sea, and Air*; American Society of Mechanical Engineers: New York, NY, USA, 2017; Volume 50831, p. V003T06A016.
41. Mohan, N.; Undeland, T.M.; Robbins, W.P. *Power Electronics: Converters. Applications and Design*; Wiley: Hoboken, NJ, USA, 1989.
42. Gavagnin, G.; Sánchez, D.; Rodríguez, J.M.; Muñoz AMartínez, G.S. Economic competitiveness of Dish-MGT Solar Power Generators. In Proceedings of the ASME Turbo Expo 2017: Turbomachinery Technical Conference and Exposition GT2017, Charlotte, NC, USA, 26–30 June 2017.
43. Spinelli, F.; Cogliani, E.; Maccari Aand Milone, M. La Misura e la Stima della Radiazione Solare: L'Archivio dell'ENEA e il Sito Internet Dell'Atlante Italiano della Radiazione Solare per la Pubblicazione dei Dati, Rapporto Tecnico ENEA SOL/RS/2007/21. 2007. Available online: http://www.solaritaly.enea.it/Documentazione/Archivio%20Radiazione%20e%20Solaritaly.pdf (accessed on 17 December 2021).
44. Gavagnin, G.; Sanchez, D.; Martinez, G.S.; Rodriguez, J.M.; Munoz, A. Cost analysis of solar thermal power generators based on parabolic dish and micro gas turbine: Manufacturing, transportation and installation. *Appl. Energy* **2017**, *194*, 108–122. [CrossRef]